THE ASTROPHYSICAL JOURNAL, 355:102–113, 1990 May 20

A MEASUREMENT OF THE TEMPERATURE OF THE COSMIC MICROWAVE BACKGROUND AT A FREQUENCY OF 7.5 GHz

A. KOGUT, M. BENSADOUN, G. DE AMICI, S. LEVIN, G. F. SMOOT, AND C. WITEBSKY
University of California, Berkeley, Lawrence Berkeley Laboratory, and Space Sciences Laboratory
Received 1989 July 11; accepted 1989 November 15

ABSTRACT

We have measured the intensity of the cosmic microwave background (CMB) at a frequency of 7.5 GHz (wavelength 4.0 cm) using a ground-based, total power radiometer calibrated at the antenna aperture by an external cryogenic reference target. The radiometer measured the difference in antenna temperature between the reference target and the zenith sky from a dry, high-altitude site. Subtraction of foreground signals (primarily atmospheric and galactic emission) measured with the same instrument leaves the CMB as the residual. The radiometer measured the atmospheric antenna temperature by correlating the signal change with the air mass in the beam during tip scans. The small galactic signal was subtracted based on extrapolation from lower frequencies and was checked by differential drift scans. The limiting uncertainty in the CMB measurement was the effect of ground radiation in the antenna sidelobes during atmospheric measurements. The thermodynamic temperature of the CMB at 7.5 GHz is 2.60 ± 0.07 K (68% confidence level).

Subject headings: cosmic background radiation — Earth: atmospheres

I. INTRODUCTION

The cosmic microwave background (CMB) is widely interpreted as a relic of a hot, dense phase in the early universe. Radiative processes at redshifts greater than $z_{obs} \sim 2.2 \times 10^6 \Omega_b^{-1/3} h_{50}^{-2/3}$ efficiently thermalize an arbitrary initial CMB spectrum to a Planck spectrum (Danese and De Zotti 1982), where Ω_b is the baryon density relative to the closure density and h_{50} is the Hubble constant in units of 50 km s^{-1} Mpc^{-1}. Energy releases to the matter or radiation fields at epochs more recent than z_{obs} will distort the CMB spectrum from a Planckian distribution, with the size and shape of the distortion dependent on the details and epoch of the energy release.

Matsumoto *et al.* (1988) report a distortion at sub-millimeter wavelengths. The excess flux has been variously interpreted in terms of Compton distortions or dust emission from an early generation of stars (e.g., Hayakawa *et al.* 1988; Adams *et al.* 1989 and references therein). The CMB spectrum in the Rayleigh-Jeans region ($\lambda > 1$ cm) can help distinguish among competing models for the submillimeter excess. In addition, the long-wavelength spectrum may contain distortions unrelated to the apparent excess in the Wien region.

As part of an ongoing effort to characterize the Rayleigh-Jeans CMB spectrum, we have measured the CMB intensity at a number of frequencies from a high-altitude site (Smoot *et al.* 1985, 1987). Our results limited potential energy releases to $\delta E/E \leq 1\%$ at redshifts between z_{obs} and $\sim 4 \times 10^4$ (Smoot *et al.* 1988). The weighted mean of ground-based results, however, differed from measurements using other techniques (e.g., Johnson and Wilkinson 1986; Crane *et al.* 1986). In an effort to alter and reduce potential systematics common to recent ground-based results, we returned to our high-altitude site in late summer 1988 with a new cryogenic reference target, improved instruments at 1.5 and 3.8 GHz, and a new radiometer operating at 7.5 GHz. This paper details the measurement at 7.5 GHz.

II. CONCEPT OF THE MEASUREMENT

We measure the CMB spectrum with a radiometer, a device whose output voltage is proportional to the microwave power intercepted by the input port. In the Rayleigh-Jeans region, signals are commonly quoted in units of antenna temperature T_A, related to the power emitted by a blackbody completely filling the antenna aperture by

$$T_A = \frac{P}{kB} = \frac{x}{e^x - 1} T , \quad (1)$$

where P is the received power, k is Boltzmann's constant, B is the bandwidth of the observation, T is thermodynamic temperature, and x is the dimensionless frequency

$$x = \frac{h\nu}{kT} .$$

Here h is Planck's constant and ν is the frequency. The experiment compares the output voltage as the radiometer alternately views the zenith sky and a cryogenic reference target ("cold load") with a well-determined antenna temperature. The antenna temperature of the zenith sky, $T_{A,\text{zenith}}$, is then determined by the voltage difference and the calibration constant G of the radiometer,

$$T_{A,\text{zenith}} - T_{A,\text{load}} = G(S_{\text{zenith}} - S_{\text{load}}) , \quad (2)$$

where $T_{A,\text{load}}$ is the antenna temperature of the cold load, S_{zenith} and S_{load} refer to the output voltage as the radiometer views the zenith and the cold load, respectively. The zenith antenna temperature is the sum of many signals:

$$T_{A,\text{zenith}} = T_{A,\text{CMB}} + T_{A,\text{Atmm}} + T_{A,\text{Gal}} + T_{A,\text{Ground}} + T_{A,\text{RFI}} + \Delta T_{\text{Offset}} , \quad (3)$$

where $T_{A,\text{CMB}}$ is the antenna temperature of the CMB, $T_{A,\text{Atm}}$ is the antenna temperature of the atmosphere, $T_{A,\text{Gal}}$ is the

antenna temperature of the Galaxy, $T_{A,\mathrm{Ground}}$ is the antenna temperature of the Earth seen in the antenna sidelobes, $T_{A,\mathrm{RFI}}$ is the antenna temperature of man-made radio-frequency interference (RFI), and $\Delta T_{\mathrm{Offset}}$ is a correction for any systematic changes in radiometer performance (reflection, insertion loss, system temperature) in the interval between viewing the zenith and the cold load. Radiation from the Sun and Moon is easily avoided by observing only when these sources are below the horizon. Equations (2) and (3) can be solved for the CMB temperature:

$$T_{A,\mathrm{CMB}} = G(S_{\mathrm{zenith}} - S_{\mathrm{load}}) + T_{A,\mathrm{load}} - T_{A,\mathrm{Atm}} - T_{A,\mathrm{Gal}} - T_{A,\mathrm{Ground}} - T_{A,\mathrm{RFI}} - \Delta T_{\mathrm{Offset}} . \quad (4)$$

We calculated $T_{A,\mathrm{load}}$ based on the known and measured properties of the materials used in the reference target; to first order, it is simply the boiling temperature of the liquid helium (LHe) cryogen. We measured directly all other terms in equation (4) using the same instrument as for the zenith sky measurement. Tipping the radiometer a fixed amount and correlating the increased signal with the increased air mass in the beam measured the atmospheric antenna temperature. The minor galactic contribution is estimated from extrapolations of maps at lower frequencies and checked by differential drift scans. We estimated $T_{A,\mathrm{Ground}}$ based on the measured far-field beam pattern and on tests that modulated the radiation in the antenna sidelobes.

We performed the measurements from the Nello Pace Laboratory of the University of California's White Mountain Research Station. The station is located on a high mountain plateau (elevation 3800 m) in the rain shadow of the Sierra Nevada range in eastern California (latitude 37°.5 N). Typical column densities of precipitable water vapor during clear summer nights are in the range 2–5 mm H_2O. The magnitude and variability of the atmospheric signal from the laboratory are approximately a factor of 3 smaller than from sea level in Berkeley. The station is also remote from man-made radio sources, which preclude operation of the instrument near major population centers.

III. DESCRIPTION OF THE INSTRUMENT

a) The Radiometer

The radiometer is a direct-gain, total-power receiver with a corrugated conical horn antenna on the input port. The RF chain is shown in Figure 1. The antenna is the same one used for measurements at 10 GHz (Kogut *et al.* 1988) with a new circular-to-rectangular waveguide transition optimized for operation at 7.5 GHz. An isolator on the input of the first amplifier prevented impedance-dependent offset changes. The amplified and rectified signal underwent an additional amplification of 2500 in a DC amplifier, which integrated the signal for a period of 2 s. The amplified DC signal was digitized and recorded every 2 s by the same multiplexer/ADC used by the 10 GHz radiometer in previous years. The 7.5 GHz radiometer shared the system in 1988 with radiometers operating at frequencies of 1.5, 3.8, and 90 GHz. Table 1 summarizes the properties of the radiometer.

b) The Reference Target

The largest term in equation (4) is the antenna temperature of the reference load, $T_{A,\mathrm{load}}$. Between 1987 and 1988 we built a new reference target optimized for use between 1 and 10 GHz (Fig. 2). It consisted of a microwave absorber (Emerson &

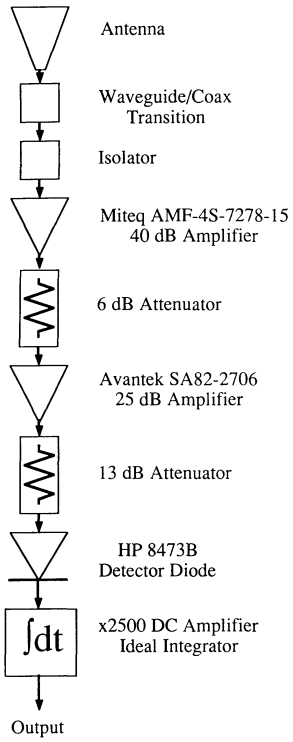

FIG. 1.—Schematic of the RF chain

Cumings EHP-12 backed by E&C LS) submerged in LHe within a large upright cryostat. The radiometer mated with the target at the horn aperture through an ambient temperature, RF-tight metal plate at the cryostat top. A fiberglass-backed aluminum foil cylinder surrounded the absorber and acted as an oversized multimode waveguide ("radiometric wall") to minimize emission from warm portions of the cryostat. Two (23 μm) polyethylene windows at the top of the cryostat prevented air from condensing on the radiometric wall and adding to its emissivity. A fraction of the helium boil-off gas, heated above ambient temperature, circulated between the polyethylene windows to prevent the formation of water condensation or frost on the top window. Two (76 and 152 μm) Teflon-impregnated glass cloth (Fluorglas 381-3) windows served as low-pass filters, blocking the infrared (IR) heat leak to the microwave absorber. The windows had large absorption in the IR but were essentially transparent below 10 GHz (opacity $\tau \leq 2 \times 10^{-4}$ at 7.5 GHz).

Although similar to the reference load used in previous years, the new cold load incorporated several important changes. The Fluorglas windows replaced a cumbersome

TABLE 1

PROPERTIES OF THE RADIOMETER

Parameter	Value
Passband	7.25–7.75 GHz
System temperature	234 ± 3 K
Broadcast temperature	302 ± 1 K
Sensitivity	0.011 K Hz$^{-1/2}$ (Predicted)
	0.044 K Hz$^{-1/2}$ (Measured)
Calibration	49.2 K/V
Beam FWHM	20° ± 2°

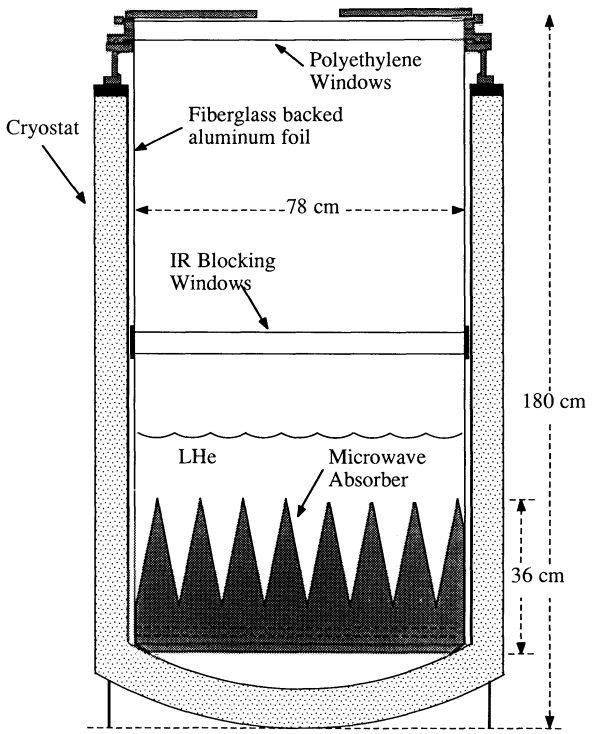

FIG. 2.—Schematic of the cryogenic reference target

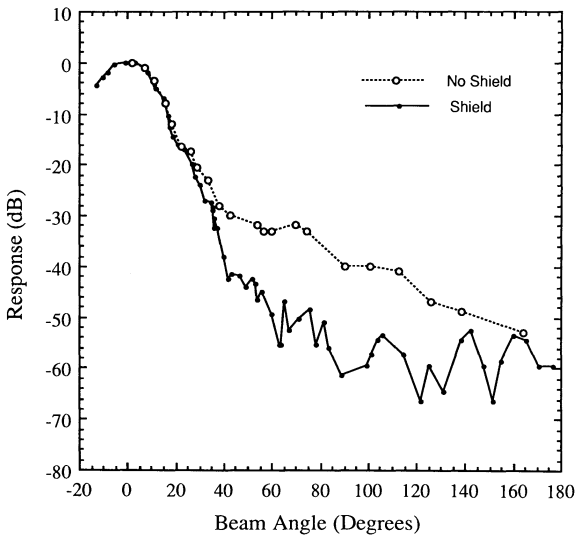

FIG. 3.—Far-field E-plane beam pattern of the antenna, measured with (*closed circles*) and without (*open circles*) the ground shield.

shutter. The new absorber was 50% thicker, and the radiometric wall slightly wider in diameter. The transition from the top flange to the radiometric wall was simplified and made smoother, with no steps or gaps larger than 0.5 mm. A series of sensors behind the radiometric wall allowed better estimation of the cryogen level and the temperature profile in the radiometric wall.

The measured pressure within the cold load in 1988 was 485 ± 2 mm Hg, corresponding to a LHe boiling point (thermodynamic temperature) of 3.778 ± 0.004 K (Duriex and Rusby 1983). Corrections for reflected and emitted power are small (<0.020 K). The contributions to $T_{A,\mathrm{load}}$ are summarized in Appendix A. We took the antenna temperature of the reference target in 1988 to be $T_{A,\mathrm{load}} = 3.621 \pm 0.009$ K.

c) *Ambient Target*

We calibrated the radiometer by comparing the voltage difference as the radiometer viewed two known, dissimilar targets: the cryogenic reference target and a small ambient target. The ambient target consisted of a slab of microwave absorber (Eccosorb CV-3) 25 cm × 25 cm × 8 cm, enclosed in a metal box insulated by 2.5 cm of closed-cell foam. The target could be opened to cover the antenna aperture completely and was otherwise left closed to allow the interior to thermalize. A thermistor within the Eccosorb monitored the target temperature.

d) *Ground Shield*

We measured the antenna to have a half-power beam width of $20 \pm 2°$ at 7.5 GHz. We built a large pyramidal ground shield that attached to the radiometer during atmospheric scans and the measurement of $T_{A,\mathrm{zenith}}$. The height and position of the shield were such that beam angles smaller than 35° viewed the sky directly, while larger angles were reflected by the shield. A flared section with flare radius of two wavelengths reduced diffraction over the edges of the shield. The far-field beam pattern of the corrugated horn antenna is shown in Figure 3. The contribution of the ground shield can be seen at beam angles greater than 35°, where the shield added between 10 and 20 dB additional rejection of the ground signal. Emission from the shield was small (<0.001 K).

IV. SYSTEM PERFORMANCE TESTS

We performed numerous tests on site at White Mountain to assess the magnitude of effects contributing to the error budget of the measurement.

a) *Systematic Changes*

The entire experiment depended upon the radiometer's response remaining independent of its orientation. We tested extensively to place limits on this effect. The radiometer may be modeled as an ideal radiometer with a system temperature T_{system}, power absorption coefficient A, and power reflection coefficient R, observing a target at temperature T_{Target}. Neglecting terms second-order in A and R, the output voltage is

$$S = \frac{1}{G}\left[T_{\mathrm{Target}} + T_{\mathrm{system}} + R(T_{\mathrm{Broadcast}} - T_{\mathrm{Target}}) + A(T_{\mathrm{int}} - T_{\mathrm{Target}})\right], \quad (5)$$

where T_{int} is the temperature of the internal absorbing component and $T_{\mathrm{Broadcast}}$ is the antenna temperature of the power emitted by the radiometer (in this case, equal to the temperature of the isolator on the input). Changes in the calibration constant G, the system temperature, or the reflection or absorption coefficients will produce a voltage change, which will be detected if it is systematically correlated with radiometer position.

In the simplest test, we clamped the ambient calibration target firmly over the antenna aperture, then repeatedly changed the radiometer's position while recording the output. These tests were sensitive to changes in radiometer calibration constant or system temperature, but were not particularly sen-

TABLE 2

POSITION-DEPENDENT EFFECTS

	Δ(180)[a]	Δ(−40)	Δ(−30)	Δ(+30)	Δ(+40)
Ambient	−26 ± 2	20 ± 7	2 ± 2	−1 ± 3	2 ± 4
LN	−52 ± 17	...	...	...	...
$\Delta T_{\rm Offset}$	−52 ± 34	20 ± 7	2 ± 2	−1 ± 3	2 ± 4

[a] $\Delta(\theta)$ is the difference $G(S_{\rm zenith} - S_\theta)$, in mK. A positive result means the zenith appears warmer than angle θ. 180° is the down position looking into the cold load.

sitive to changes in insertion loss or reflection coefficient of the components in the RF chain. To test for these effects, the radiometer must view a target with temperature significantly different from the broadcast temperature and the temperature of the RF components. For this purpose we used a small liquid nitrogen (LN) target, which consisted of a disk of microwave absorber (Eccosorb CV-3 backed by two layers of Eccosorb AN-72) in a metal cylinder closed on one end. The target fitted neatly over the antenna aperture, with the metal cylinder preventing side or backlobe reception of the ground signal. Dipped in LN, inverted until the liquid had largely ceased to drip from the Eccosorb tips, and then placed over the antenna aperture, the target proved to be stable in temperature in any orientation for periods greater than 32 s.

Table 2 shows the results of the tests performed at Barcroft, for both ambient and LN targets. Since all the measurements were differential, we have arbitrarily taken the effect at zenith to be the zero point of the tests. The results were generally consistent from day to day and had noise levels consistent with control runs in which the radiometer did not move. The only nonzero effect appeared when the radiometer was inverted. With an ambient target over the antenna, the radiometer output was 0.026 ± 0.002 K colder when the radiometer pointed down. With a LN target replacing the ambient target, the effect grew to 0.052 ± 0.034 K. The relatively large uncertainty of the LN result precluded precise identification of the term in equation (5) responsible for the effect.

Two other sources of uncertainty needed to be considered: that the LN target itself changed temperature in a position-dependent fashion (e.g., from LN dripping from the absorber tips), or that additional effects could arise when the radiometer mated with the cold load (e.g., from reflections at the horn mouth). We placed limits on both possibilities by comparing the output signal as the radiometer alternately viewed the cold load (with LN cryogen), the LN flip target (in both up and down orientations), and the zenith sky (a convenient stable load). We observed no effect at the 0.030 K level. This systematic uncertainty has been included in the total uncertainty of the LN tests above.

The LN target approximated a 4 K load better than the ambient target; consequently, we chose to use the results of the LN test, unscaled, to correct the measured signal difference between the cold load and the zenith sky. The resultant correction $\Delta T_{\rm Offset}$ in equation (4) was then $\Delta T_{\rm Offset} = -0.052 \pm 0.034$ K.

b) *Sidelobe Reception*

The ground was the brightest source in the vicinity of the radiometer. Although its contribution was greatly reduced by the corrugated horn antenna, ground radiation entering the antenna sidelobes could still contribute a large, angle-dependent signal to the upward-pointing radiometer, systematically altering the determinations of both $T_{A,\rm zenith}$ and $T_{A,\rm Atm}$. We estimated the contribution of $T_{A,\rm Ground}$ in several ways.

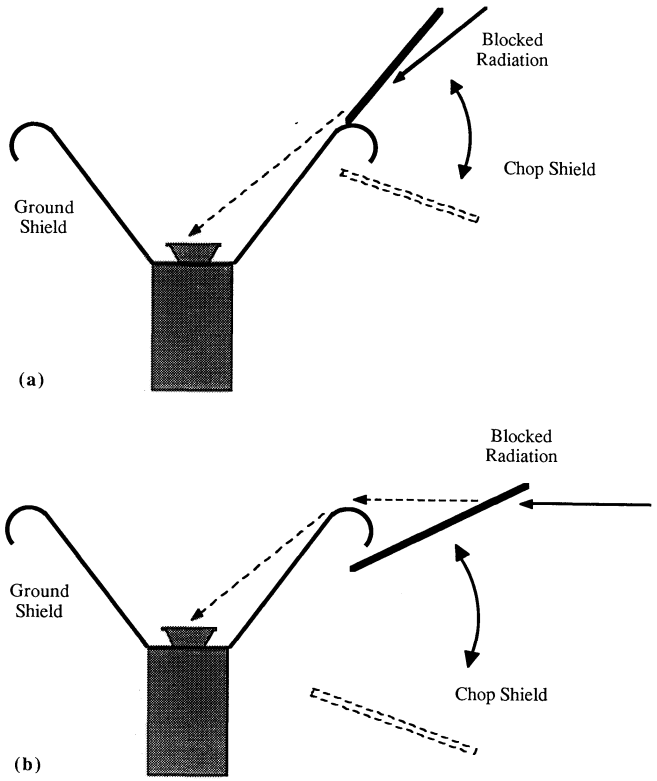

FIG. 4.—Schematic representation of the tests used to set lower limits on $T_{A,\rm Ground}$. The aluminum chop shield was alternately placed to block a radiation path, then removed.

We obtained a lower limit on $T_{A,\rm Ground}$ by alternately adding and removing a large piece of sheet metal to one side of the ground shield. The simplest test used the additional "chop" shield as an extension of the ground shield. If ground radiation were entering the antenna beam without diffracting, the chop shield would block some fraction of this radiation, replacing it with reflected sky radiation (Fig. 4*a*). We recorded the output voltage and searched for signals synchronous with the chop period. The local horizon rose sharply to the west and was visible in the main antenna lobe above the ground shield for the −40° and −30° positions. A similar test searched for radiation diffracting over the flared sections. In this case, the chop shield undercut the flares, replacing ground radiation with reflected sky radiation in the vicinity of the flares (Fig. 4*b*). A small diffraction signal was evident in the E-plane at all angles. We obtained only null results from the H-plane rests. Resuts of these tests are summarized in Table 3.

The measured far-field E-plane beam pattern convolved with a flat blackbody horizon yielded an upper limit on $T_{A,\rm Ground}$, provided the contribution from areas near the radiometer was adequately described by the far-field beam pattern. Although the ground was within 1.5 m of the horn aperture, and thus within the near field of the horn alone, we measured the far-field beam pattern with the pyramidal ground shield in place over the horn. The diffraction pattern over the flared shield sections should have been independent of source distance provided the source was several wavelengths from the

TABLE 3

ESTIMATED $T_{A,\mathrm{Ground}}$

	−40° (mK)	−30° (mK)	Zenith (mK)	+30° (mK)	+40° (mK)
Lower limit from measurements	96 ± 15	24^{+14}_{-4}	3^{+8}_{-3}	5^{+5}_{-2}	10^{+5}_{-2}
Upper limit from beam pattern	...	...	23 ± 5	36 ± 5	47 ± 10
Estimated $T_{A,\mathrm{Ground}}$	125 ± 23[a]	45 ± 18	13 ± 10	21 ± 15	29 ± 18
$\Delta T_{A,\mathrm{Ground}}(\theta - \mathrm{zenith})$	112 ± 19	32 ± 16	...	8 ± 8	16 ± 13

[a] The higher horizon to the west rises above the ground shield. The estimated $T_{A,\mathrm{Ground}}$ for −40° and −30° is given by the value for the corresponding eastern angle plus the lower limit measured for the western angles.

flares; hence, the response of the horn/shield combination was adequately described by the measured far-field beam pattern (i.e., the ground shield acted as a reflecting surface, not a continuation of the horn antenna). We concluded that ground emission with the horn/shield combination could be modeled to better accuracy than with the horn alone.

The value of $T_{A,\mathrm{Ground}}$ measured by chop tests was somewhat lower than the value expected from the beam pattern. The two results could be reconciled if the direct sidelobe tests did not modulate the entire ground signal, or if the H-plane beam pattern provided significantly more rejection of the ground signal than the E-plane. We treated the direct tests as a lower limit to $T_{A,\mathrm{Ground}}$, and the beam pattern convolution as an upper limit. We took as the estimate of $T_{A,\mathrm{Ground}}$ the arithmetic mean of the two methods, with an uncertainty equal to half the spread between them. A substantial fraction of $T_{A,\mathrm{Ground}}$ was a constant arising from the response at large angles ($\geq 130°$) which always viewed the ground for any of the radiometer positions used. This contribution did not change as the radiometer tipped; hence, the differential uncertainty in $T_{A,\mathrm{Ground}}$ between the zenith and 40° was somewhat less than the absolute uncertainty at either position. The estimated values for $T_{A,\mathrm{Ground}}$, both absolute and differential, are summarized in Table 3. We used these values in equation (4) and in the calculation of $T_{A,\mathrm{Atm}}$.

c) *Calibration Stability*

An ideal total-power radiometer viewing a target of antenna temperature T_{Target} for an integration time τ has rms noise described by

$$\Delta T_{\mathrm{noise}} = [T_{\mathrm{system}} + T_{\mathrm{Target}}]\left[\frac{1}{B\tau} + \left(\frac{\delta G}{G}\right)^2\right]^{1/2}$$

(Kraus 1969). If gain fluctuations $\delta G/G$ are negligible, the noise is Gaussian and decreases as the inverse square root of the integration time. The measured noise was larger than predicted and decreased approximately as $\tau^{-1/2}$ on time scales shorter than 64 s (Table 1). On longer time scales the noise increased slightly from its minimum value. Observations of stable targets (4 K and ambient) showed non-Gaussian fluctuations in gain to be the dominant source of noise in the instrument. We averaged stable data into blocks 24 s in duration separated by a time Δt, and looked for changes in the rms between successive blocks as the time delay Δt was increased. The 24 s integration time and time delay Δt between 32 and 112 s corresponded to the time scales typical of the atmosphere and zenith sky measurements. The noise increased as $\Delta t^{0.4 \pm 0.1}$ and was larger when viewing the ambient target by a factor 1.8 ± 0.1. Both were consistent with a random-walk process in the calibration coefficient of the radiometer, with variations $\delta G/G \sim 10^{-4}$ on time scales of several minutes.

Data analysis included removal of a linear drift in calibration over the course of a single scan. We analyzed control runs of stable data as though they were atmospheric or zenith sky measurements; the resultant data sets had zero mean and rms noise of 0.020–0.030 K. We concluded that fluctuations in radiometer calibration dominated the system noise, but served only to inject additional noise at the 0.020–0.030 K level and did not systematically alter the signal differences.

d) *Calibration Linearity*

The major source of nonlinear behavior in the RF chain was the HP 8473B detector diode. The radiometer design deliberately kept the RF gain low to keep the diode in the linear regime for all but the ambient target. Scans measuring $T_{A,\mathrm{zenith}}$ and $T_{A,\mathrm{Atm}}$ calculated the calibration coefficient G using the ambient–LHe or ambient-sky signal difference, which was slightly saturated. We corrected the calibration of the radiometer by pointing it at three targets in rapid succession: the reference target, the LN target, and an ambient target. From the three targets, three calibration coefficients may be determined. The ratio of calibrations determined by LHe–LN to LHe–ambient targets fixed the correction to be applied to the LHe–ambient scan calibrations for saturation effects at 0.985 ± 0.005.

e) *RFI*

Another unwanted contribution to the sky signal was RFI. Near Berkeley, commercial and government microwave communication links raised $T_{A,\mathrm{zenith}}$ to over 50 K. The situation was considerably better at a remote location; nevertheless, we searched for RFI at Barcroft before beginning any other tests. With a spectrum analyzer replacing the detector diode, we observed no RFI at 10 kHz resolution over the range 5.75–8.75 GHz, corresponding to a limit on RFI contributions of $T_{A,\mathrm{RFI}} < 0.005$ K at any of the angles used.

f) *Pointing*

Systematic differences between the zenith angle θ used in atmospheric analysis and the true zenith angle θ' of the radiometer could alter the calculated $T_{A,\mathrm{Atm}}$ from the true value. We measured the pointing of the radiometer repeatedly and found it to be quite stable (Table 4). The bubble clinometer used to establish the absolute pointing has an uncertainty of $\pm 5'$ in its zero point, which dominated the pointing uncertainty.

TABLE 4

MEASURED POINTING

Nominal Angle	−40°	−30°	−15°	Zenith	+15°	+30°	+40°
Mean Angle	−40°19′	−30°22′	−15°29′	−0°42′	+14°31′	+29°43′	+40°4′
Single-run rms	1′	1′	2′	2′	1′	2′	2′
Total 1988 rms	8′	8′	3′	2′	2′	2′	6′

V. DATA COLLECTION AND ANALYSIS

a) *Calibration Coefficient*

We calculated the calibration coefficient G of the radiometer by recording the voltage difference as the radiometer viewed the ambient and cryogenic targets and correcting for nonlinearity:

$$G = \beta \frac{T_{A,\mathrm{Amb}} - T_{A,\mathrm{load}}}{S_{\mathrm{Amb}} - S_{\mathrm{load}}}, \tag{6}$$

where $T_{A,\mathrm{Amb}}$ is the antenna temperature of the ambient target and S_{Amb} and S_{load} are the output voltages viewing the ambient target and cold load, respectively. We adopted a value for the saturation correction β of 0.985 ± 0.005 (§ IV*d*). For atmospheric and galactic measurements the zenith sky substituted for the cold load, with equation (6) solved iteratively to achieve self-consistency. All analysis used a linear interpolation between successive measurements of G to reduce the effect of slow changes in absolute calibration. Residual scatter of successive measurements of G varied by $\delta G/G < 10^{-4}$.

b) *Atmosphere*

For a radiometer with a pencil beam viewing an optically thin, planar atmosphere, $T_{A,\mathrm{Atm}}$ may be calculated by the relation

$$T_{A,\mathrm{Atm}} = G \frac{S_\theta - S_{\mathrm{zenith}}}{\sec(\theta) - \sec(0)}$$

$$= G \frac{S_\theta - S_{\mathrm{zenith}}}{\sec(\theta) - 1}, \tag{7}$$

where S_θ and S_{zenith} are the outputs of the radiometer viewing angle θ and the zenith, respectively. In fact, the above model is somewhat simplistic. The real atmosphere is curved to follow the Earth's curvature; the beam pattern of the antenna has a nonnegligible width of about 20°; the atmospheric opacity causes a slight self-absorption of the signal. The generalization of equation (7) is

$$T_{A,\mathrm{atm}} \cong \frac{\Delta T_{\mathrm{Atm}}}{F_0}\left[F_1 + \left(\frac{\Delta T_{\mathrm{Atm}}}{F_0\, T_{\mathrm{kin}}}\right)F_2 + \left(\frac{\Delta T_{\mathrm{Atm}}}{F_0\, T_{\mathrm{kin}}}\right)^2 F_3\right], \tag{8}$$

(e.g., Witebsky *et al.* 1987; De Amici *et al.* 1985), where ΔT_{Atm} is the antenna temperature of the signal difference,

$$\Delta T_{\mathrm{Atm}} = G(S_\theta - S_{\mathrm{zenith}}),$$

T_{kin} is the physical temperature of the atmosphere ($\sim$240 K), and F_0, F_1, F_2, and F_3 are moments of the measured beam pattern convolved with a curved atmospheric shell, evaluated numerically using the measured far-field E-plane beam pattern with the ground shield in place. We determined $T_{A,\mathrm{Atm}}$ from equation (8) on a scan-by-scan basis, after correcting ΔT_{Atm} for the differential effects of $\Delta T_{\mathrm{Offset}}$, $T_{A,\mathrm{Ground}}$, and $T_{A,\mathrm{Galaxy}}$.

The radiometer scanned in the E-plane to angles of 30° and 40° on either side of the zenith along the E–W ($\pm 1°$ azimuth) direction. The ground shield remained firmly attached to the radiometer throughout the entire measurement. The radiometer viewed the following targets in sequence for 32 s each: the sky at each of the positions −40° (W), −30°, zenith, +30°, and +40° (E), followed by the ambient target. Sixteen seconds elapsed before and after observation of the ambient target, during which time we ignored the data. A single atmospheric scan took 224 s. The maximum elapsed time between measurements of the zenith and any angle θ was 32 s. An atmospheric run typically lasted an hour and comprised 10 to 15 complete scans. We measured $T_{A,\mathrm{Atm}}$ on the nights of 1988 September 3, 4, 5, 7, 9, 11, 14, 15, 16, 17, and 19.

The linear interpolation for G removed the major effects of gain drifts during the course of a single scan. Nonlinear changes large enough to effect the estimate of $T_{A,\mathrm{Atm}}$ occurred rarely. The pattern of the sky observations (western angles first followed by the zenith and the eastern angles) provided a distinctive signature for such processes. Residual drifts in $G(t)$ on time scales of a single scan typically added a signal ΔS to the west-zenith signal difference, and a signal $-\Delta S$ to the east-zenith signal difference, which occurred in the opposite time order. The calculated values for $T_{A,\mathrm{Atm}}$ should be displaced by roughly equal amounts above and below the mean value. We observed this signature in 10 of the 285 total scans. The suspect scans were discarded.

c) *Zenith Sky*

We calculated $T_{A,\mathrm{zenith}}$ using equation (2) on a scan-by-scan basis. The radiometer observed the cold load for 32 s, the zenith for 16 s, and the ambient target for 16 s. Sixteen seconds elapsed between each position, during which time we discarded all data. A complete scan sequence took 128 s, with only 16 s separating the observations of the cold load and the zenith sky. A typical observing run over the cold load lasted 40 minutes and comprised some 15 independent measurements of $T_{A,\mathrm{zenith}}$. We obtained 65 independent measurements of measured $T_{A,\mathrm{zenith}}$ on 1988 September 16, 17, and 19.

d) *Galaxy*

We corrected the $T_{A,\mathrm{CMB}}$ and $T_{A,\mathrm{Atm}}$ for the minor galactic contribution based on a model extrapolated from 408 MHz maps of Haslam *et al.* (1982), scaled by a position-independent spectral index of −2.75, and a compilation of thermal sources at 2.7 GHz, with spectral index −2.1. We checked the model by comparing the signals when the radiometer pointed 15° east and west of zenith, corresponding to two positions at declination 36° separated by 2.4 hours in right ascension (R.A.). We measured the differential galactic profile on the nights of 1988 September 5, 6, 8, and 10, observed simultaneously with four radiometers at 1.5, 3.8, 7.5, and 90 GHz.

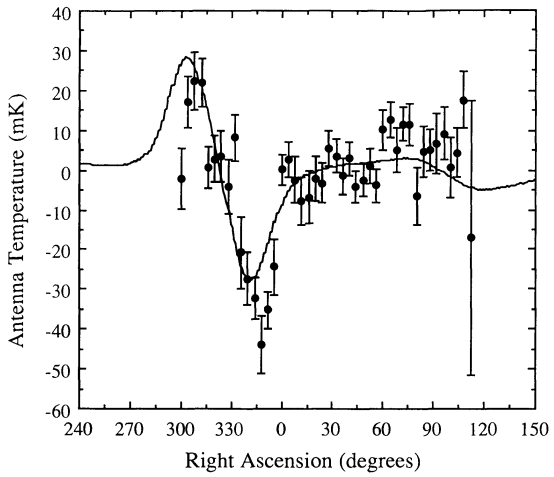

FIG. 5.—Observed differential galactic profile (*points*) and the signal predicted from extrapolation of maps at lower frequencies (*solid line*).

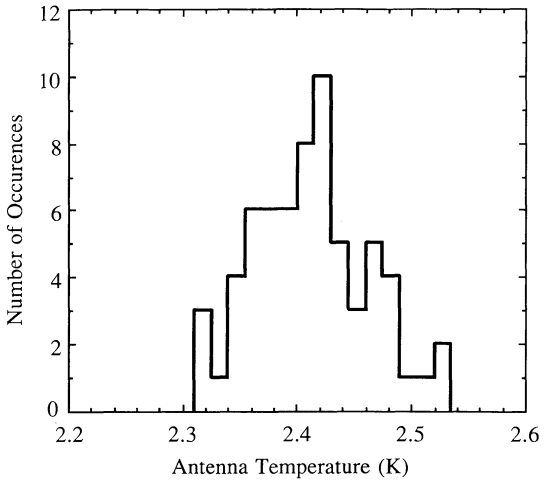

FIG. 6.—Histogram of 65 independent measurements of $T_{A,\mathrm{CMB}}$

The measured galactic signal at 7.5 GHz lay within 0.010 K of the predicted signal (Fig. 5). The maximum error entailed in subtracting $T_{A,\mathrm{Gal}}$ is 0.05 K in $T_{A,\mathrm{Atm}}$ for those few scans in which the galactic plane crossed the zenith during observations. Uncertainties in the galactic signal off the plane of the galaxy (i.e., during most of our atmosphere scans and all of the CMB scans) were smaller (0.005 K).

VI. RESULTS

a) $T_{A,\mathrm{Atm}}$

The values for $T_{A,\mathrm{Atm}}$ at each of the four scan angles are presented in Table 5 for all nights in which we measured $T_{A,\mathrm{zenith}}$. The angles to the west had a large correction for $T_{A,\mathrm{Ground}}$; the mean value for $T_{A,\mathrm{Atm}}$ included data from the eastern (+) angles exclusively. Atmospheric temperatures at the eastern angles were in excellent agreement with each other; $T_{A,\mathrm{Atm}}$ measured at +40° was 0.020 ± 0.012 K warmer than the value measured at 30°. The data at 30° had a mean rms scatter of 0.221 K, while the rms at 40° was 0.162 K. This noise was consistent with the small fluctuations in the calibration constant discussed in § IV*c*, multiplied by the [secant $(\theta) - 1]^{-1}$ angular dependence of the atmospheric signal differences, and approximated a Gaussian distribution within each hour-long observing run.

The error budget for each atmospheric angle is given in Table 6. Systematic corrections are presented as an additive correction to $T_{A,\mathrm{Atm}}$. The uncertainties in $T_{A,\mathrm{Ground}}$, $\Delta T_{\mathrm{Offset}}$, and $T_{A,\mathrm{Ground}}$ have been multiplied by the [secant $(\theta) - 1]^{-1}$ angular dependence of the atmospheric signal differences for each of the four angles. All the terms in Table 6 have been measured; the associated uncertainties represent the 68% confidence level of the measurement.

b) $T_{A,\mathrm{CMB}}$

We determined $T_{A,\mathrm{CMB}}$ by solving equation (4) on a scan-by-scan basis (Table 7). We did not measure $T_{A,\mathrm{Atm}}$ concurrently with $T_{A,\mathrm{zenith}}$; instead, we used the values for $T_{A,\mathrm{Atm}}$ from each night fitted to a linear drift. As we did not observe the atmosphere to vary dramatically throughout any night, the uncertainty in $T_{A,\mathrm{CMB}}$ incurred in the atmospheric interpolation was small. The values of $T_{A,\mathrm{CMB}}$ from the four runs are in good agreement, showing no more variation than would be expected from noise. The individual values for $T_{A,\mathrm{CMB}}$ had a Gaussian distribution (Fig. 6). The rms width of the distribution was

TABLE 5

MEASURED $T_{A,\mathrm{Atm}}$[a]

Date (1989)	Time (UT)	−40° (mK)	−30° (mK)	+30° (mK)	+40° (mK)	Mean $T_{A,\mathrm{Atm}}$ (mK)
Sep 16.....	3:15–4:18	1301 ± 44	1134 ± 57	1078 ± 48	1113 ± 55	1100 ± 49
	5:03–5:28	1113 ± 37	900 ± 62	1166 ± 50	1158 ± 32	1162 ± 39
	6:29–7:05	1123 ± 53	879 ± 75	1055 ± 79	1133 ± 49	1094 ± 62
	7:42–8:15	1215 ± 58	983 ± 105	1201 ± 49	1177 ± 34	1189 ± 31
	9:24–10:01	1139 ± 53	1008 ± 44	1160 ± 67	1113 ± 43	1137 ± 49
	11:46–12:12	1213 ± 38	894 ± 48	1035 ± 58	1091 ± 37	1064 ± 45
Sep 17.....	8:26–9:03	1127 ± 43	838 ± 64	1245 ± 63	1243 ± 40	1244 ± 48
	10:18–11:02	1098 ± 41	869 ± 84	1081 ± 58	1160 ± 26	1121 ± 39
	12:38–13:08	1129 ± 56	808 ± 80	913 ± 86	990 ± 35	952 ± 57
Sep 19.....	9:07–10:03	...[b]	...	1046 ± 42	1095 ± 24	1071 ± 31
	11:02–11:48	...	...	1088 ± 43	1080 ± 34	1084 ± 33

[a] $T_{A,\mathrm{Atm}}$ has been corrected for systematic effects; however, the quoted uncertainties are statistical only. Systematic uncertainties are summarized in Table 6.

[b] We observed only the eastern angles on September 19.

TABLE 6

CORRECTIONS TO $T_{A,\mathrm{Atm}}$[a]

Effect	−40 (mK)	−30 (mK)	+30 (mK)	+40 (mK)
$T_{A,\mathrm{Ground}}$	−359 ± 61	−201 ± 101	−52 ± 52	−52 ± 42
$\Delta T_{\mathrm{Offset}}$	+64 ± 22	+12 ± 12	−6 ± 20	+6 ± 13
$T_{A,\mathrm{Galaxy}}$	0 ± 10	0 ± 18	0 ± 18	0 ± 10
Beam pattern	0 ± 14	0 ± 14	0 ± 14	0 ± 14
Pointing	0 ± 7	0 ± 7	0 ± 7	0 ± 7
Absolute gain	0 ± 4	0 ± 4	0 ± 4	0 ± 4
Total systematic correction	−295 ± 68	−189 ± 105	−58 ± 61	−46 ± 48
Statistical uncertainty	47	69	59	37
Total uncertainty	83	126	85	61

[a] Systematic corrections for each angle have been multiplied by the $[\sec(\theta) - 1]^{-1}$ factor; the uncertainties have been added in quadrature. The statistical uncertainty for each angle is the mean value from all scans Sep 16–19.

0.050 K with 65 data points; consequently, we adopted 0.006 K as the estimate of the statistical uncertainty in the mean value of $T_{A,\mathrm{CMB}}$.

The estimated error budget for the CMB measurement is given in Table 8. The systematic uncertainty of 0.066 K was dominated by the uncertainty in the largest foreground signal, the atmosphere. Adding the systematic uncertainty in quadrature with the statistical uncertainty, we obtained a value for the antenna temperature of the CMB of

$$T_{A,\mathrm{CMB}} = 2.421 \pm 0.067 \text{ K (68\% C.L.)}$$

Using equation (1) to convert this value to thermodynamic temperature yielded the final result at 7.5 GHz of

$$T_{\mathrm{CMB}} = 2.60 \pm 0.07 \text{ K} .$$

VIII. DISCUSSION

a) $T_{A,\mathrm{Atm}}$

The atmosphere at low frequencies is not completely understood. The dominant component of atmospheric emission below 10 GHz is continuum O_2 emission, with a minor, variable contribution from water vapor. Models of atmospheric emission with water vapor content typical of our high-altitude site (2–5 mm H_2O) predict $T_{A,\mathrm{Atm}}$ at 7.5 GHz in the range 0.89–0.96 K (Liebe, Manabe, and Hufford 1988; Liebe 1981, 1985). The mean $T_{A,\mathrm{Atm}}$ at 7.5 GHz measured during LHe observations was 1.08 ± 0.06 K. From day to day, we observed rms scatter of ~0.07 K. Both the magnitude and variability of this signal were slightly larger than predicted.

An increase in signal magnitude and variability compared to modeled atmospheric emission is a feature common to several recent low-frequency measurements of the atmosphere (e.g., Kogut *et al.* 1988; De Amici *et al.* 1988). In general, the model parameters are fitted to the line features of the emission peaks and may be much poorer descriptions of the windows of astrophysical interest. Several corrections to the contribution from the O_2 continuum and the 22 GHz water line have been proposed (e.g., Danese and Partridge 1989 and references therein), which tend to increase the signal magnitude and variability below 10 GHz. The resultant variability in $T_{A,\mathrm{Atm}}$ at 7.5 GHz is in better (but still poor) agreement with the observed signal variability.

The value of $T_{A,\mathrm{Atm}}$ at 7.5 can be compared to measurements from White Mountain at nearby frequencies. Results from 3.8, 7.5, and 10.0 GHz are summarized in Table 9. The model of atmospheric emission predicts $T_{A,\mathrm{Atm}}$ at 7.5 GHz to be smaller than at 10 GHz by 0.100–0.150 K, and larger than 3.8 GHz by 0.080–0.130 K. The observed differences were 0.100 and 0.125 K, respectively, in agreement with the model differences if not the magnitudes. One is led to the conclusion that, at frequencies below 10 GHz, the data are better understood than the atmospheric model.

b) T_{CMB}

Table 10 lists recent precise CMB measurements, shown in Figure 7. The measurement at 7.5 GHz is in excellent agreement with other ground-based results, which in turn are in poor agreement with measurements at higher frequencies using other techniques. The mean of all ground-based measurements since 1965, weighted by their uncertainties, is 2.658 ± 0.029 K ($\chi^2 = 13.9$ for 22 DOF), compared to the weighted mean of 2.786 ± 0.013 K ($\chi^2 = 6.4/7$ DOF) for all other measurements

TABLE 7

MEASURED VALUES FOR $T_{A,\mathrm{CMB}}$[a]

Date	Time (UT)	Number of Scans	Calibration (K/V)	$G(S_{\mathrm{zenith}} - S_{\mathrm{load}})$ (K)	$T_{A,\mathrm{Atm}}$ (K)	$T_{A,\mathrm{CMB}}$ (K)
Sep 16.....	5:45–6:15	16	48.978 ± 0.003	−0.107 ± 0.010	1.097 ± 0.025	2.434 ± 0.010
Sep 16.....	8:28–9:13	21	48.585 ± 0.007	−0.147 ± 0.011	1.085 ± 0.025	2.412 ± 0.011
Sep 17.....	11:45–12:07	11	48.166 ± 0.013	−0.123 ± 0.013	1.071 ± 0.025	2.450 ± 0.014
Sep 19.....	10:13–10:47	17	48.234 ± 0.013	−0.163 ± 0.012	1.078 ± 0.025	2.402 ± 0.012
All scans		65	...	...	1.083 ± 0.012	2.421 ± 0.006

[a] Although $T_{A,\mathrm{Atm}}$ and $T_{A,\mathrm{CMB}}$ have been corrected for $T_{A,\mathrm{Galaxy}}$, $T_{A,\mathrm{Ground}}$, and $\Delta T_{\mathrm{Offset}}$, the quoted uncertainties are statistical only, to allow comparison of data between days. Systematic uncertainties are listed in Table 6 for $T_{A,\mathrm{Atm}}$ and Table 8 for $T_{A,\mathrm{CMB}}$.

TABLE 8

CONTRIBUTIONS TO CMB ERROR BUDGET[a]

Effect	Typical Magnitude	Uncertainty in $T_{A,CMB}$ (mK)
$T_{A,Atm}$	1083 ± 55 mK	55
ΔT_{Offset}	-52 ± 34 mK	34
$T_{A,Ground}$	13 ± 10 mK	10
$T_{A,Load}$	3621 ± 9 mK	9
$T_{A,Galaxy}$	10 ± 5 mK	5
$T_{A,RFI}$	0 ± 5 mK	5
Calibration	48.585 ± 0.007 K/V	<1
Total systematics	...	66
Statistical uncertainty	...	6
Total uncertainty	...	67

[a] All uncertainties are 68% confidence level estimates.

TABLE 9

COMPARISON OF $T_{A,ATM}$[a]

Year	3.8 GHz	7.5 GHz	10 GHz
1986	870 ± 108	...	1200 ± 65
1987	898 ± 74	...	1160 ± 83
1988	955 ± 55	1083 ± 55	...
Model	810–830	890–960	990–1120

[a] The quoted uncertainties are 68% confidence level and include systematic effects. Model predictions assume a range of precipitable water vapor between 2 and 5 mm.

below 0.1 cm. The weighted average is a valid estimate of the mean of the parent distribution, provided the uncertainties are uncorrelated and no spectral features are present. In fact, the ground-based measurements share to some extent a number of systematic uncertainties, most notably in the measurement of the atmosphere. The CN results, too, share some fraction of the

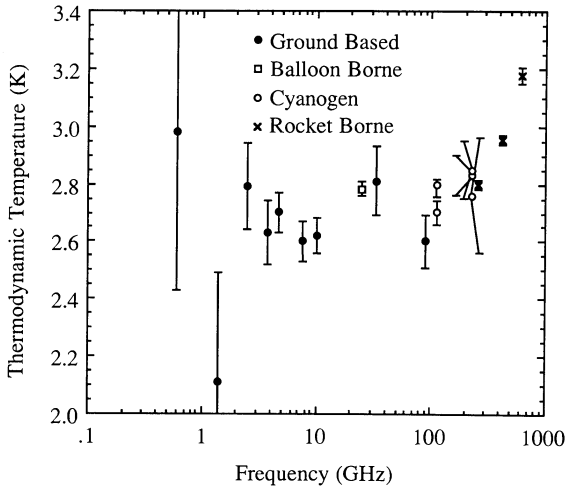

FIG. 7.—Recent precise CMB measurements

systematic uncertainty. That the weighted uncertainties are thus underestimated to some extent does not alter the fact that ground-based measurements report results whose average is systematically lower than other techniques. One is led to the conclusion that either set of measurements has undetected systematics, or that additional spectral features may exist in the Rayleigh-Jeans portion of the CMB spectrum. The low-frequency (≤ 10 GHz) CMB spectrum has been observed solely by ground-based measurements and has not been tested by a method with radically different systematics. In a field with a history of unsuspected systematic effects, confirmation of any suspected spectral feature should be obtained by as many methods as possible. A balloon-borne spectral measurement between 1 and 10 GHz would be of great interest in resolving the question of possible CMB distortions below 3 cm.

TABLE 10

RECENT CMB MEASUREMENTS[a]

Reference	Wavelenth (cm)	Frequency (GHz)	TCMB (K)	Technique[b]
Sironi *et al.* 1987	50.0	0.6	2.98 ± 0.55	GB
Levin *et al.* 1988	21.3	1.41	2.11 ± 0.38	GB
Sironi and Bonelli 1986	12.0	2.5	2.79 ± 0.15	GB
De Amici (Levin *et al.* 1989)	7.9	3.8	2.63 ± 0.11	GB
Mandolesi *et al.* 1986	6.3	4.75	2.70 ± 0.07	GB
Kogut *et al.* 1990[c]	4.0	7.5	2.60 ± 0.07	GB
Kogut (Levin *et al.* 1989)	3.0	10.0	2.62 ± 0.06	GB
Johnson and Wilkinson 1986	1.2	24.8	2.783 ± 0.025	BB
De Amici *et al.* 1985	0.909	33.0	2.81 ± 0.12	GB
Bersanelli *et al.* 1989	0.333	90.0	2.60 ± 0.09	GB
Meyer and Jura 1985	0.264	113.6	2.70 ± 0.04	CN
	0.132	227.3	2.76 ± 0.20	CN
Crane *et al.* 1988	0.264	113.6	$2.796^{+0.019}_{-0.041}$	CN
	0.132	227.3	2.85 ± 0.10	CN
Meyer *et al.* 1989	0.132	227.3	2.83 ± 0.07	CN
Matsumoto *et al.* 1988	0.116	259	2.799 ± 0.018	R
	0.0709	423	2.955 ± 0.017	R
	0.0481	624	3.175 ± 0.027	R

[a] For a review of data prior to 1980, see Weiss 1980.

[b] "GB" indicates a ground-based measurement, "BB" a balloon-borne measurement, "CN" a spectroscopic measurement using the CN molecule, and "R" a rocket-borne experiment.

[c] This work.

IX. CONCLUSIONS

We have measured the brightness temperature of the CMB at frequency 7.5 GHz to be 2.60 ± 0.07 K. The largest contribution to the uncertainty of the measurement is the contribution of diffracted ground radiation entering the antenna sidelobes during tip scans to measure the antenna temperature of the atmosphere. The weighted mean of all ground-based CMB measurements appears systematically lower than measurements at higher frequencies using other techniques. The apparent conflict can be resolved by postulating undetected systematics in either set of measurements, or a possible CMB distortion at wavelengths below ~ 3 cm.

This experiment could never have occurred without the skilled help of many people. We wish to thank Jon Aymon, John Gibson, Jenny Hwang, Jay Levin, Larry Levin, Faye Mitschang, Luis Tenorio, and the staff and crew of the White Mountain Research Station for their assistance. This work was supported by NSF grant DPP-8716548 and by the Department of Energy under contract DE-AC03-76SF000098.

APPENDIX A

ANTENNA TEMPERATURE OF THE REFERENCE TARGET

The reference target/radiometer combination may be modeled without loss of generality as a perfect radiometer observing a perfect absorber, with a series of reflecting and absorbing surfaces between them. The antenna temperature of the load is then the sum of the power emitted by the load (attenuated by the surfaces between the load and the radiometer) and the power broadcast by the radiometer and reflected back by the load (in practice, the attenuation is negligible). We will consider these two terms independently.

a) Reflection

The reflection coefficient of the cold load is the coherent sum of the individual amplitude reflection coefficients. Radiation reflecting from surfaces within a coherence length L of the radiometer can interfere coherently with the broadcast radiation. We include this effect as an effective phase term for each reflecting surface, where the phase of reflections internal to the radiometer has been selected as the reference phase. The amplitude reflection coefficient r of the cold load is thus

$$r = r_R + r_{F1}e^{i\phi F1} + r_{F2}e^{i\phi F2} + r_H e^{i\phi H} + r_A e^{i\phi A} + r_{P1}e^{i\phi P1} + r_{P2}e^{i\phi P2} + r_T e^{i\phi T} ,$$

where subscripts R, F, H, A, P, and T refer to the radiometer, Fluorglas windows, helium liquid/gas interface, microwave absorber, polyethylene windows, and transition from horn to radiometric cavity, respectively. The magnitudes of the last three terms are small, and may be neglected with negligible error:

$$r \approx r_R + r_{F1}e^{i\phi F1} + r_{F2}e^{i\phi F2} + r_H e^{i\phi H} + r_A e^{i\phi A} . \tag{A1}$$

The reflected signal is proportional to the square of the reflection coefficient and the difference in broadcast temperature between the radiometer and the cold load,

$$\Delta T_{\rm ref} \approx |r|^2 (T_{\rm Broad} - T_{\rm Abs}) ,$$

where the temperature of the load to lowest order is simply the temperature of the absorber. Squaring equation (A1) gives the sum

$$\begin{aligned} |r|^2 = {} & |r_R|^2 + |r_{F1}|^2 + |r_{F2}|^2 + |r_H|^2 + |r_A|^2 \\ & + 2r_R r_{F1} \cos(\phi_{F1}) \\ & + 2r_R r_{F2} \cos(\phi_{F2}) \\ & + 2r_R r_H \cos(\phi_H) \\ & + 2r_R r_A \cos(\phi_A) \\ & + 2r_{F1} r_{F2} \cos(\phi_{F1} - \phi_{F2}) \\ & + 2r_{F1} r_H \cos(\phi_{F1} - \phi_H) \\ & + 2r_{F1} r_A \cos(\phi_{F1} - \phi_A) \\ & + 2r_{F2} r_H \cos(\phi_{F2} - \phi_H) \\ & + 2r_{F2} r_A \cos(\phi_{F2} - \phi_A) \\ & + 2r_H r_A \cos(\phi_H - \phi_A) . \end{aligned} \tag{A2}$$

Equation (A2) is valid for radiation coherent over regions much larger than the separations between any two surfaces. In practice, the 500 MHz bandwidth B of the radiometer implies a coherence length $\Lambda = c/B = 60$ cm, comparable to the separations involved. Over distances $x \sim \Lambda$, the phase coherence diminishes by an amount $\zeta(z)$,

$$\zeta(z) = \left[\frac{\sin(z)}{z}\right]^2 ,$$

where the phase difference z is related to the separation x between two surfaces by

$$z = \frac{2\pi x}{\Lambda} .$$

Each cosine term in equation (A2) must be multiplied by the function $\zeta(z)$ applicable for the separation between the reflecting surfaces.

In addition, there is an effect from illumination. The horn antenna occupies $\sim 6\%$ of the aperture of the load; in addition, the radiometer beam diverges as the distance from the horn mouth increases. Only a fraction Γ of the power broadcast from the radiometer and reflecting from a surface actually reenters the antenna; the rest reflects from the top plate and is absorbed by the microwave absorber. Each term in equation (A2) must also be multiplied by the illumination Γ of the reflecting surface. With these corrections, the reflection coefficient of the reference load may be written as

$$\begin{aligned} |r|^2 = {} & |r_R|^2 + |r_{F1}|^2\Gamma_{F1} + |r_{F2}|^2\Gamma_{F2} + |r_H|^2\Gamma_H + |r_A|^2\Gamma_A \\ & + 2r_R r_{F1} \cos(\phi_{F1})\Gamma_{F1}\zeta(z_{F1}) \\ & + 2r_R r_{F2} \cos(\phi_{F2})\Gamma_{F2}\zeta(z_{F2}) \\ & + 2r_R r_H \cos(\phi_H)\Gamma_H\zeta(z_H) \\ & + 2r_R r_A \cos(\phi_A)\Gamma_A\zeta(z_A) \\ & + 2r_{F1} r_{F2} \cos(\phi_{F1} - \phi_{F2})\Gamma_{F1}\zeta(z_{F1,F2}) \\ & + 2r_{F1} r_H \cos(\phi_{F1} - \phi_H)\Gamma_{F1}\zeta(z_{F1,H}) \\ & + 2r_{F1} r_A \cos(\phi_{F1} - \phi_A)\Gamma_{F1}\zeta(z_{F1,H}) \\ & + 2r_{F2} r_H \cos(\phi_{F2} - \phi_H)\Gamma_{F2}\zeta(z_{F2,H}) \\ & + 2r_{F2} r_A \cos(\phi_{F2} - \phi_A)\Gamma_{F2}\zeta(z_{F2,H}) \\ & + 2r_H r_A \cos(\phi_H - \phi_A)\Gamma_H\zeta(z_{H,A}) . \end{aligned} \tag{A3}$$

All terms contributing to equation (A3) are listed in Table 11A. Equation (A3) consists of a constant term (proportional to the summed power reflectivity of each surface and the illuminations), a term dependent on the product of the amplitude coefficients of the radiometer and reflecting surfaces (modulated by the phase ϕ between the radiometer and the reference load), and a term dependent

TABLE 11A

REFLECTION PROPERTIES

	Position[a] (cm)	r[b]	Γ	$\zeta(z)$
Radiometer (R)	0.0	0.1	1.0	...
Top IR window ($F1$)	111	6.5×10^{-3}	7.9×10^{-2}	7×10^{-3}
Bottom IR window ($F2$)	116	1.3×10^{-2}	7.9×10^{-2}	7×10^{-3}
LHe interface (H)	156	1.2×10^{-2}	2.1×10^{-2}	4×10^{-3}
Absorber (A)	162	3.2×10^{-3}	2.1×10^{-2}	4×10^{-3}
$F1$-$F2$	...	...	...	0.9
$F1$-H	...	...	...	5×10^{-2}
$F1$-A	...	...	...	4×10^{-2}
$F2$-H	...	...	...	6×10^{-2}
$F2$-A	...	...	...	4×10^{-2}
H-A	...	...	...	0.9

[a] The throat of the horn has been taken as the reference for position and phase.
[b] Amplitude reflection coefficient.

TABLE 11B

EMISSION PROPERTIES

Material	Emissivity	Temperature (K)	Emission (mK)
Polyethylene	2.4×10^{-6}	270	0.7
Top IR window	4.9×10^{-5}	50 ± 35[a]	2.5
Bottom IR window	9.9×10^{-5}	30 ± 25	3.0
Radiometric wall	$\sim 10^{-4}$	4–270	<1
Joints	1.0	30, 50	6
Total	...	...	13 ± 7 mK

[a] The uncertainty for the window temperatures includes drifts caused by fluctuations in cryogen level over the course of the measurements.

on the amplitude reflection coefficients within the load (modulated by their separation). The power reflection internal to the radiometer, $|r_R|^2$, may be neglected as it cancels in the sky—load comparison (provided $T_{A,\text{zenith}}$ is not greatly different from $T_{A,\text{Load}}$).

The phase-independent terms sum to $\sum |r_i|^2\Gamma_i = 2.0 \times 10^{-5}$. Multiplied by the 298 K temperature difference between the radiometer's broadcast temperature and the absorber temperature, these terms contribute 6 ± 3 mK to $T_{A,\text{Load}}$.

Terms dependent on the single-phase ϕ_i between the radiometer and the ith reflecting surface can be calculated knowing the positions of each surface. The terms are small: were all of the terms to add coherently, the reflection dependent on radiometer position would sum to less than 1 mK. As a precaution, we tested for this effect by sliding the radiometer on a specially constructed extension of the radiometric wall. We observed no signal while changing the phases ϕ_i by more than 4π. Terms dependent on the radiometer's position contribute 0 ± 1 mK to $T_{A,\text{Load}}$.

Of the remaining terms, only the first has an appreciable magnitude. The term

$$2r_{F1}r_{F2} \cos(\phi_{F1} - \phi_{F2})\Gamma_{F1}\zeta(z_{F1,F2})$$

represents coherent reflection between the two Fluorglas IR-blocking windows. The windows are spaced 5 cm apart; consequently, the phase term between them has a nominal value -1. In practice, we cannot be sure that gas pressure does not force the windows closer together. We take this term to be 0 ± 4 mK instead of the nominal -4 mK. Including the 3 mK power reflection from the polyethylene windows (neglected after equation [A1]) gives the total estimated reflected power of 6 ± 5 mK.

b) Emission

Emission properties of the reference load are summarized in Table 11B. The temperatures for the Fluorglas windows are taken from sensors on the radiometric wall where the windows attach. The IR heat load may heat the windows to a somewhat higher temperature; this uncertainty dominates the uncertainty from window emission.

The 78 cm diameter radiometric wall is a good approximation to free space. We estimate emission from the false wall by convolving the far-field beam pattern with the radiometric wall, using the emissivity of a 25 μm aluminum layer. The aluminum foil contributes less than 1 mK to $T_{A,\text{Load}}$. In addition, there are two joints in the radiometric wall at the locations of the Fluorglas windows. Modeling emission from the joints as blackbody gives an upper limit to their contribution of 6 mK. We estimated the total contribution to $T_{A,\text{load}}$ from emission of warm parts of the load as 13 ± 7 mK. Drifts in window or joint temperature caused by fluctuations in cryogen level are included in this uncertainty.

The microwave absorber has an emissivity greater than 0.999. Its thermodynamic temperature is that of the liquid helium bath. At the ambient pressure of 485 ± 2 mm Hg, helium boils at 3.778 ± 0.004 K. Converting to antenna temperature at 7.5 GHz and adding the minor reflection and emission terms gives the final value for the reference temperature:

$$T_{A,\text{Load}} = 3.621 \pm 0.009 \text{ K} .$$

REFERENCES

Adams, F. C., Freese, K., Levin, J., and McDowell, J. C. 1989, *Ap. J.*, **344**, 24.
Bersanelli, M., Witebsky, C., Bensadoun, M., De Amici, G., Kogut, A., Levin, S., and Smoot, G. 1989, *Ap. J.*, **339**, 632.
Crane, P., Heygi, D. J., Mandolesi, N., and Danks, A. 1986, *Ap. J.*, **309**, 822.
Crane, P., Heygi, D. J., Kutner, M., and Mandolesi, N. 1988, *Proc. Third ESO/CERN Symposium*, ed. M. Caffo, R. Fanti, G. Giacomelli, and A. Renzini (Dordrecht: Kluwer), in press.
Danese, L., and De Zotti, G. 1978, *Astr. Ap.*, **68**, 157.
———. 1980, *Astr. Ap.*, **84**, 364.
———. 1982, *Astr. Ap.*, **107**, 39.
Danese, L., and Partridge, R. B. 1989, *Ap. J.*, **342**, 604.
De Amici, G., Smoot, G., Aymon, J., Bersanelli, M., Kogut, A., Levin, S., and Witebsky, C. 1988, *Ap. J.*, **329**, 556.
De Amici, G., Smoot, G., Friedman, S. D., and Witebsky, C. 1985, *Ap. J.*, **298**, 710.
Duriex, M., and Rusby, R. L. 1983, *Metrologia*, **19**, 67.
Haslam, C. G. T., Salter, C. J., Stoffel, H., and Wilson, W. E. 1982, *Astr. Ap. Suppl.*, **47**, 1.
Hayakawa, S., Matsumoto, T., Matsuo, H., Murakami, H., Sato, S., Lange, A., and Richards, P. L. 1988, *Pub. Astr. Soc. Japan*, **39**, 941.
Johnson, D. G., and Wilkinson, D. T. 1986, *Ap. J. (Letters)*, **313**, L1.
Kogut, A., Bersanelli, M., De Amici, G., Friedman, S. D., Griffith, M., Grossan, B., Levin, S., Smoot, G. F., and Witebsky, C. 1988, *Ap. J.*, **235**, 1.
Kraus, J. D. 1966, *Radio Astronomy* (New York: McGraw-Hill), pp. 241–244.
Levin, S. M., Witebsky, C., Bensadoun, M., Bersanelli, M., De Amici, G., Kogut, A., and Smoot, G. F. 1988, *Ap. J.*, **334**, 14.
Levin, S. M., Bensadoun, M., Bersanelli, M., De Amici, G., Kogut, A., Smoot, G. F., and Witebsky, C. 1989, *Particle Astrophysics: Forefront Experimental Issues*, ed. E. Norman (Singapore: World Scientific).
Liebe, H. J. 1981, *Radio Sci.*, **16**, 1183.
———. 1985, *Radio Sci.*, **20**, 1069.
Liebe, H. J., Manabe, T., and Hufford, G. A. 1988, *IEEE Trans.*, submitted.
Mandolesi, N., Calzolari, P., Cortiglioni, S., and Morigi, G. 1986, *Ap. J.*, **310**, 561.
Matsumoto, T., Hayakawa, S., Matsuo, H., Murakami, H., Sato, S., Lange, A. E., and Richards, P. L. 1988, *Ap. J.*, **329**, 567.
Meyer, D. M., and Jura, M. 1985, *Ap. J.*, **297**, 119.
Meyer, D. M., Roth, K. C., and Hawkins, I. 1989, *Ap. J. (Letters)*, **344**, L1.
Sironi, G., and Bonelli, G. 1986, *Ap. J.*, **311**, 418.
Sironi, G. *et al.* 1987, *Proc 13th Texas Symposium on Relativistic Astrophysics*, ed. M. P. Ulmer (Singapore: World Scientific).
Smoot, G., *et al.* 1985, *Ap. J. (Letters)*, **291**, L23.
Smoot, G., Bensadoun, M., Bersanelli, M., De Amici, G., Kogut, A., Levin, S., and Witebsky, C. 1987, *Ap. J. (Letters)*, **317**, L45.
Smoot, G., Levin, M., Witebsky, C., De Amici, G., and Rephaeli, Y. 1988, *Ap. J.*, **331**, 653.
Sunyaev, R. A., and Zel'dovich, Ya. B. 1970, *Ap. Space Sci.*, **7**, 20.
Weiss, R. 1980, *Ann. Rev. Astr. Ap.*, **18**, 489.
Witebsky, C., Smoot, G., De Amici, G., and Friedman, S. D. 1986, *Ap. J.*, **310**, 145.
Zel'dovich, Ya. B., and Sunyaev, R. A. 1969, *Ap. Space Sci.*, **4**, 301.

A. KOGUT: Laboratory for Astronomy and Solar Physics, Code 685.3, NASA Goddard Space Flight Center, Greenbelt, MD 20771

M. BENSADOUN, G. DE AMICI, S. LEVIN, G. F. SMOOT, and C. WITEBSKY: 50/232 Lawrence Berkeley Laboratory, University of California, Berkeley, CA 94720